

# CLAS12 Reconstruction Resolution

A. Saina,<sup>1</sup> V. Ziegler,<sup>2</sup> R. Sanford,<sup>3</sup> and G.P. Gilfoyle<sup>3</sup>

<sup>1</sup>*University of Surrey, Guilford, UK*

<sup>2</sup>*Jefferson Lab, Newport News, VA*

<sup>3</sup>*University of Richmond, Richmond, VA*

August 15, 2022

## Abstract

The CEBAF Large Acceptance Spectrometer at 12 GeV (CLAS12) in Hall B at Jefferson Lab is a mass spectrometer capable of detecting both charged and neutral particles over a large fraction of the full solid angle. The data is processed by the CLAS12 Analysis and Reconstruction Architecture, CLARA. Signals from different detectors are matched together into a trajectory through CLAS12. The aim of this study was to obtain the resolution of the event reconstruction software in simulation. To extract the resolutions, generated and reconstructed track parameters of particles were used as starting points and directions for a particle swimmer. The two tracks were propagated to the surfaces of the subsystems comprising the CLAS12 Forward Detector. The differences in positions and angles of the two tracks at the detector surfaces were plotted in histograms, the histograms fitted with gaussians and the width being a measure of the resolutions. The dependence of the resolutions on particle species and energy, the torus field polarity and the detector geometry was investigated, along with the effects of a new version of the simulation software. The resolution calculations will provide benchmark values when future upgrades are made to the software and hardware elements of the reconstruction.

## Contents

<b>1</b>	<b>Motivation</b>	<b>3</b>
<b>2</b>	<b>CLAS12 Description</b>	<b>3</b>
<b>3</b>	<b>CLAS12 Reconstruction Software</b>	<b>4</b>
<b>4</b>	<b>CLAS12 Monte-Carlo Simulation (<i>gemc</i>)</b>	<b>4</b>
<b>5</b>	<b>Method</b>	<b>5</b>
<b>6</b>	<b>Results</b>	<b>9</b>
<b>7</b>	<b>Conclusion</b>	<b>12</b>

## 1 Motivation

In this project we measure the reconstruction resolution in simulation for each of the subsystems of the CLAS12 Forward Detector (FD). This is done by swimming two simulated tracks through the CLAS12 FD. One track uses the known (or generated) vertex and initial 3-momentum from the event generator that was the input to the simulation. The second track uses the reconstructed vertex and momentum produced by the reconstruction code itself. Differences between these two tracks are used to extract the reconstruction resolution. The effects of particle energy, particle type, torus field polarity, sector dependence, and geometry were studied using two recent versions of the CLAS12, physics-based simulation code *gemc*.

These results can provide benchmarks for hardware and software development for the FD subsystems and guidance for setting goals and specifications. The micro-service architecture of Clara enables developers to quickly swap components of the reconstruction chain and the benchmarks established here can provide test goals. They can also illuminate the different contributions of software and hardware to the CLAS12 resolution and be employed in unit tests as a measure of the stability of new code.

The reconstruction code uses a Kalman filter to extract the track parameters. The results here can be used to parameterize the dependence of the resolution on various kinematic variables and incorporate this dependence into the covariance matrix for the Kalman filter state vector. At each step in the Kalman filter a new state vector is estimated with a weighted average of the track data where the weights are contained in the covariance matrix. This matrix contains both the uncertainties and their correlations and identifies which measurements should have greater weight in the calculation. The results of this study can also be used to validate the matching criteria for the outer detector subsystems.

## 2 CLAS12 Description

The Forward Detector of CLAS12 consist of six identical sectors with a toroidal field generated by superconducting coils in each sector[1]. An array of drift chambers, time-of-flight counters, Cherenkov counters, calorimeters, and other devices measure and identify the reaction products in the polar angle range  $5^\circ \leq \theta \leq 35^\circ$ . Scattered electrons and forward-going particles are detected in the FD. The High Threshold Cherenkov Counter (HTCC) (yellow in Fig. 1) with full coverage in polar angle  $5^\circ \leq \theta \leq 35^\circ$  and  $\Delta\phi = 2\pi$  coverage in azimuth is used for electron/pion discrimination. The HTCC is followed by the torus magnet (superconducting torus coils are gray in Fig. 1), and the drift chamber tracking system (DC) (light blue in Fig. 1) used to measure the charged particle trajectories and extract their momenta. Another set of Cherenkov counters (LTCC) (yellow in Fig. 1) comes next for pion/kaon discrimination. The forward time-of-flight scintillation counters (FTOF) (red-brown in Fig. 1) measure particle flight times and aid in particle identification. The electromagnetic calorimeters (EC and PCAL) (red in Fig. 1) measure the particle energy and detect neutral particles (photons and neutrons). Between the HTCC and the torus, the Forward Tagger is installed to detect electrons and photons at polar angles  $2^\circ \leq \theta \leq 5^\circ$ .

The Central Detector (CD) covers large polar angles ( $35^\circ - 125^\circ$ ) and is built around a solenoid magnet and another suite of detectors. In Figure 1 the electron beam enters from the right and impinges on the production target located in the center of the solenoid magnet. This magnet supports the CD and is shown at the right (upstream) end of CLAS12, where other detector components, Central TOF (CTOF) and Central Neutron Detector (CND) are also visible. In this project we focus on the FD. A Back-Angle-Neutron-Detector (BAND) is located upstream of the CD.

In Figure 2 the CLAS12 event event display (*ced*) shows a cross-sectional view for an outbending electron with hits in each of the CLAS12 FD subsystems along with the reconstructed track. Particles that enter the FD travel through the HTCC and then the three regions containing the drift chambers. The torus magnetic field is highest in Region 2 where the particle bends outward. The trajectory continues through a second Cherenkov counter (LTCC for pion/kaon discrimination), Forward TOF counters, and finally the electromagnetic calorimeters (PCAL/EC) for energy measurements. This combination of detector subsystems enables us to reconstruct the trajectory, momentum, and identity of scattered particles [1,3]. Some of the design specifications of the FD and CD are in Table 1 [1].

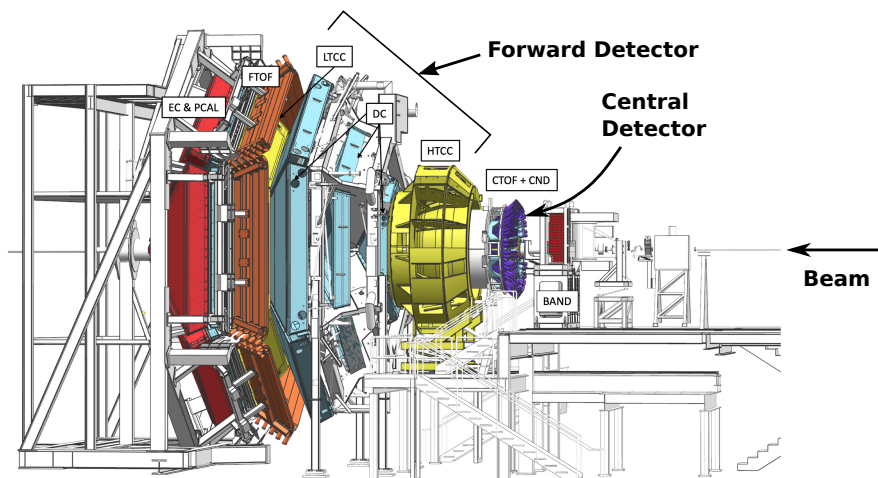


Figure 1: Representation of the CLAS12 spectrometer in Hall B at JLab. The electron beam is incident from the right side of this figure. The CLAS12 detector is roughly 13 m in scale along the beam axis. The drift chambers (DC) are marked.

	Forward Detector	Central Detector
Angular Range	5 – 35 deg	35 – 125 deg
$\delta p/p$ (%)	0.5-1.5 %	±5%
$\delta\theta$ (mrad)	1-2	2-5
$\delta\phi$ (mrad/ sin $\theta$ )	$\leq 2$	3-15
Energy (MeV)	$\geq 200$	$\geq 200$

Table 1: Summary of CLAS12 detector design parameters [1].

### 3 CLAS12 Reconstruction Software

The CLAS12 reconstruction software is based on a service-oriented architecture composed of building blocks (micro-services) that have specialized functions linked by data-stream pipes.[2, 3] Specific applications are defined by the choice of micro-services and the order of execution. The architecture is flexible so new or revised micro-services can be readily added and validated. The performance requirements are high - the expected luminosity is  $10^{35} \text{ cm}^{-2} \text{ s}^{-1}$ . CLAS12 has more than 100k readouts and runs with a trigger rate of 15k, a data rate of 600 MB/s, and live time above 95%.

The reconstruction algorithm starts with a set of hits - a detector element generates an electronic signal after passage of a charged or neutral particle [4]. These hits are grouped into clusters associated with particle trajectories and tracks are extracted in a process called hit-based tracking. At the same time energy and time measurements are processed in parallel. A micro-service, the Event Builder, sifts through the hit-based data to find the tracks and calculates the event start time when the CEBAF electron beam struck the target. With the start time in hand, another pass is made through the data using DC drift times and measured time-of-flights to produce a more accurate representation of the track. A Kalman filter is used for track fitting with a fourth-order Runge-Kutta integration method.

### 4 CLAS12 Monte-Carlo Simulation (*gemc*)

An essential tool in this project is the use of simulation to determine the reconstruction resolution for CLAS12.[5] The CLAS12 physics-based, Monte-Carlo package (*gemc*) is used to simulate the response of the detector to the passage of particles through the CLAS12 subsystems. It is built on the Geant4 package [6] which describes energy-loss and multiple scattering of particles in matter over a wide range of conditions.

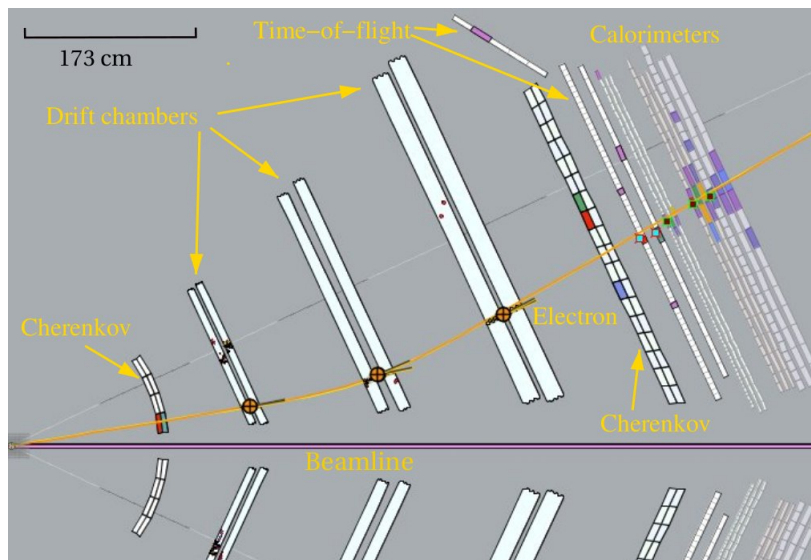


Figure 2: Cutaway view of one sector of the CLAS12 detector showing sample trajectory (entering left) as it travels through the FD. In this case the torus polarity is set so the electron bends away from the beamline due to the direction of the toroidal field.

The detector geometry is constructed with a database of Geant4 volumes created with the *genc* native API, the CLAS12 geometry service, or imported from a CAD engineering model. The energy deposited in the active volumes is digitized using plugins for each detector subsystem and is based on parameters from the CLAS12 database (CCDB). The use of databases to store geometry information and simulation parameters enables developers to do rapid prototyping without having to recompile their code. Theoretical models can be used as event generators by producing files in the LUND format which serve as input to *genc*.

## 5 Method

We now describe the procedure for measuring the reconstruction resolution for the CLAS12 Forward Detector subsystems. In Table 2 we list the subsystems and the locations where we extracted the reconstruction resolution[1]. The locations correspond to positions from the REC::Traj bank. These subsystems were

Subsystem	Measured $z$ value (cm)
High Threshold Cerenkov Counter (HTCC)	Fixed distance (175 cm) from CLAS12 origin
Drift Chambers (DC) Region 1 (R1)	layer 6 of superlayer 1
Drift Chambers (DC) Region 1 (R1)	layer 6 of superlayer 2
Drift Chambers (DC) Region 2 (R2)	layer 6 of superlayer 1
Drift Chambers (DC) Region 3 (R3)	layer 6 of superlayer 1
Forward time-of-flight (FTOF)	Panel 1a
Electromagnetic calorimeters (PCAL)	Layer 4 of EC inner

Table 2: Subsystems studied in this report.

chosen since they are essential to identifying and measuring charged-particle tracks in the FD. The quantity listed in the second column is the location of the measurement. The position of the track at this point in its trajectory is used to determine the reconstruction resolution.

We now describe the quantities used in this study and the procedure for extracting them. The observables studied here are listed in Table 3. We swim two tracks through the FD. One track uses the three-momentum of the generated event as the starting direction along with the generated vertex. The second track starts with

$\Delta x$	$\Delta y$	$\Delta z$
$\Delta \theta$	$\Delta \phi$	$b$

Table 3: Observables studied in this report. The values are in the CLAS12 laboratory coordinate system except for the HTCC. The impact parameter  $b$  is defined as  $b = \sqrt{\Delta x^2 + \Delta y^2}$ .

the reconstructed three-momentum and the reconstructed vertex. The reconstruction resolution for different observables and under different conditions is extracted by taking the difference between the two tracks and determining the effective width from those distributions. In the first row of Table 3 are the differences in the Cartesian coordinates of the intersection points of the tracks in the CLAS12 Coordinate System. These differences are taken at the positions listed in Table 2. In the second row of Table 3 are the observables  $\Delta \theta$  and  $\Delta \phi$  taken as the differences in the angles used to define the position of the intersection points in spherical coordinates. The impact parameter  $b$  will be explained in step 5 below. We now describe below the detailed steps we followed.

1. The first step in the procedure is to generate Monte-Carlo 4-vectors that are inputs to the simulation code *gemc*. The particle gun in *gemc* was used to produce data sets containing different particles, energies, and magnetic field polarities with directions distributed across different angular regions of CLAS12. The test particles are typically distributed uniformly in polar angle  $5^\circ < \theta < 35^\circ$  and azimuth  $-30^\circ < \phi < 30^\circ$  which corresponds to sector 1 in the FD. They were usually given a single, fixed energy for each simulation. These position and momentum inputs, called generated data, are the starting point for the *gemc* simulation code.
2. After passing through the *gemc* simulation the output data including both generated and simulated data was saved in High Performance Output (HIPO) format output files, the CLAS12 standard format. These data were then used as input to the CLAS12 reconstruction code and the results stored in an expanded HIPO file.
3. With these reconstructed (and generated) data in hand we next obtain two tracks that we ‘swim’ through CLAS12. We start with the generated vertex of the track and the generated 3-momentum. From this vertex a method called SectorSwim in the CLAS12 Common Tools software ‘swims’ the track through the magnetic fields created by the solenoid and the torus using a fourth-order Runge-Kutta method of integration with an adaptive step size [7]. The generated data are stored in the MC::Particle bank.
4. The second track starts with the initial 3-momentum of the reconstructed track from the reconstruction code (REC::Particle bank) at the reconstruction vertex. For both tracks the swimmer returns the state vector at the points along the trajectory stored in the REC::Traj bank for each track. The state vector consists of the Cartesian coordinates in the CLAS12 coordinate system and the 3-momentum.
5. To determine the observables in Table 3 we next rotate the track data from the CLAS12 Coordinate System to the Tilted Sector Coordinate System (TSCS) for each subsystem except the HTCC. In these coordinates, the  $z$ -axis is perpendicular to the face of the DCs, FTOF, and PCAL so the track points all lie at fixed  $z$  in the ideal geometry. We then calculate the differences between the intersection points of each track with the detector face. For the impact parameter  $b$  we calculate the magnitude of the distance between the intersection points at fixed  $z$  coordinate (*i.e.*  $b = \sqrt{\Delta x^2 + \Delta y^2}$  in the TSCS).
6. For the HTCC we extracted the observables at a fixed distance (1.75 m) from the CLAS12 origin in the CLAS12 coordinates. We used a different swimmer method with a fixed step which we adjusted so the swimmer reported the track points at the desired distance. When we used the adaptive stepsize described above in the low magnetic field in the region of the HTCC it was difficult to get track points at the desired distance.
7. We then rotate all the observables for each subsystem back to the CLAS12 Coordinate System except for the impact parameter  $b$  and the HTCC results. Since  $b$  is the distance between the generated and reconstructed tracks at fixed  $z$  it will not change under the rotation. The HTCC endpoint is not at

a fixed  $z$  coordinate so we treat it differently. After the rotation of the remaining variables we fill all histograms.

8. We use the following fitting procedure to extract the effective width from the histograms.
  - (a) The histograms for the observables typically have a wide component that covers a range of 1–3  $cm$  and has an asymmetric tail due to radiative energy loss by the particles (mostly electrons). A second, more narrow, component of the histograms has a similar mean or peak value as the wide component. For a given observable, call it  $\delta$ , we first fit the full range of the  $\delta$  histogram with a gaussian and extract the width  $\sigma_0$ , mean  $\mu_0$ , and amplitude  $A_0$ . See Figures 3-4.
  - (b) We perform an intermediate fit using the results of the previous fit to define a new gaussian restricted to the range  $\mu_0 \pm 1.5\sigma_0$  - around and near the mean  $\mu_0$  of the first gaussian. The starting values of this second fit are taken from the results of the previous fit for  $A_0$ ,  $\mu_0$ , and  $\sigma_0$ . We use the results of this step  $A_1$ ,  $\mu_1$ , and  $\sigma_1$  to set the range for the next step.
  - (c) We fit a third time using the second, intermediate fit results to set the range of the final gaussian fit to  $\mu_1 \pm 1.5\sigma_1$  - near the mean  $\mu_1$  of the second gaussian. The starting values for this fit are from that previous fit  $A_1$ ,  $\mu_1$ , and  $\sigma_1$ . The results of this third fit are  $A_2$ ,  $\mu_2$ , and  $\sigma_2$ .
  - (d) The effective width of the distribution is calculated from the variance using the results of the first and third fits. For the observable  $\delta$

$$\sigma_\delta^2 = \langle \delta^2 \rangle - \langle \delta \rangle^2$$

where [8]

$$\langle \delta^2 \rangle = \frac{A_0}{A_0 + A_2} (\mu_0^2 + \sigma_0^2) + \frac{A_2}{A_0 + A_2} (\mu_2^2 + \sigma_2^2) \quad \text{and} \quad \langle \delta \rangle = \frac{A_0}{A_0 + A_2} \mu_0 + \frac{A_2}{A_0 + A_2} \mu_2 \quad .$$

The effective widths for the different observables, subsystems, and configurations are presented as the reconstruction resolutions in Section 6.

In Figures 3-4 we show some of the histograms we generated with the procedure above and the fits to those histograms for all the observables in Table 3 for DC Region 1. Each distribution is centered near zero

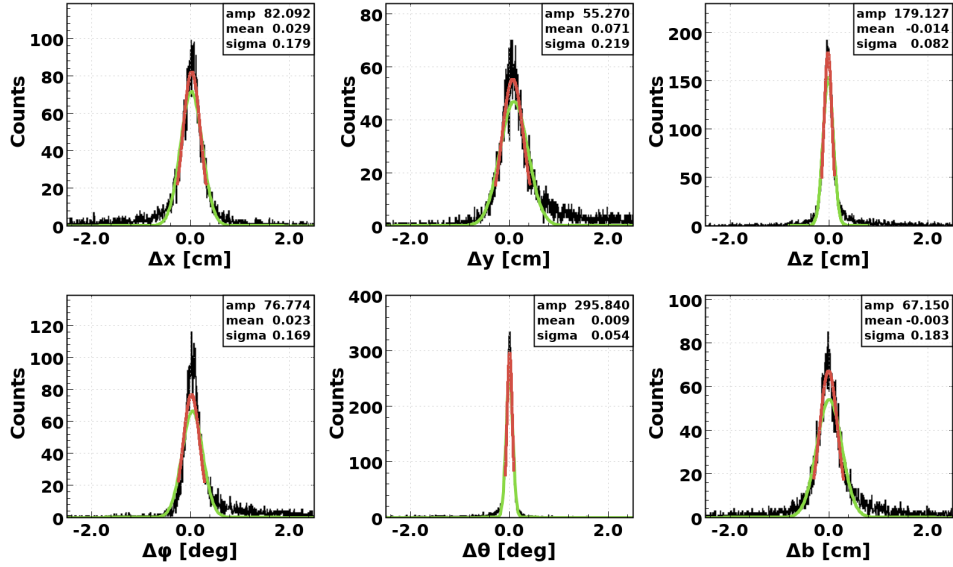


Figure 3: Histograms of the six observables with results of the fits for DC R1. The green curve is the result of the first fit to the distribution (Step 8a above). The red curve is the final fit to the narrow component. The fit parameters shown on each fit are for the red curve.

with a mean less than the width  $\sigma$  from the fit. In Figure 4 we show the distributions for all the observables in Table 3 for ECAL inner detector layer 4. As in the previous figure each distribution is centered near zero

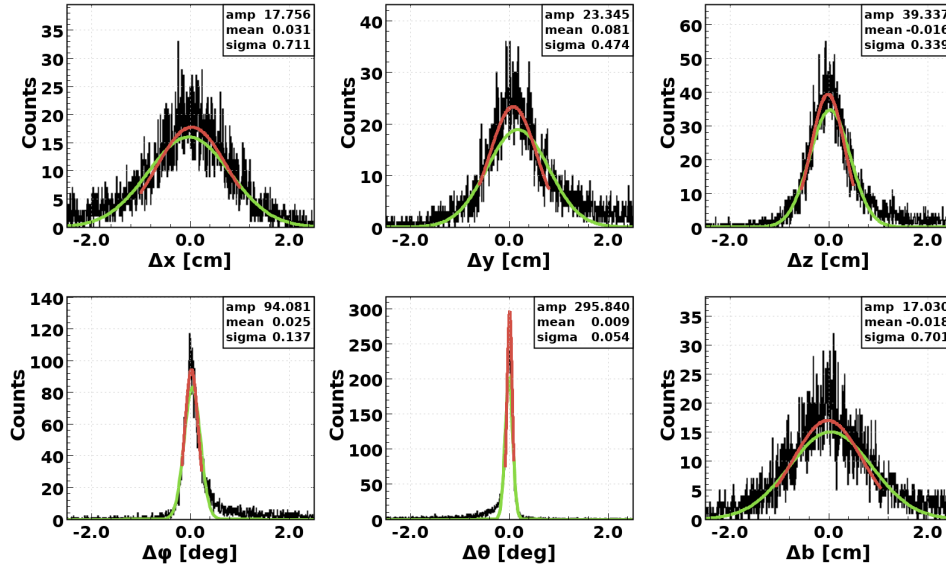


Figure 4: Histograms of the six observables with results of the fits for ECAL inner detector layer 4. The green curve is the result of the first fit to the entire distribution (Step 8a above). The red curve is the final fit to the narrow component. The fit parameters shown on each fit are for the red curve.

with a mean less than the width  $\sigma$  from the fit.

In extracting each of the observables in the different FD subsystem we swim the tracks in the TSCS, calculate the observables, and then rotate back to CLAS12 lab coordinates where the distributions are fitted as described above. Figure 5 shows results from the steps in the fitting procedure for  $\Delta\theta$ . From left to right each set of points at fixed  $z$  corresponds to the DC R1, DC R2, DC R3, FTOF, and ECAL inner detector layer 4. The top row of yellow points are the results for the resolution/width of the  $\Delta\theta$  distribution for

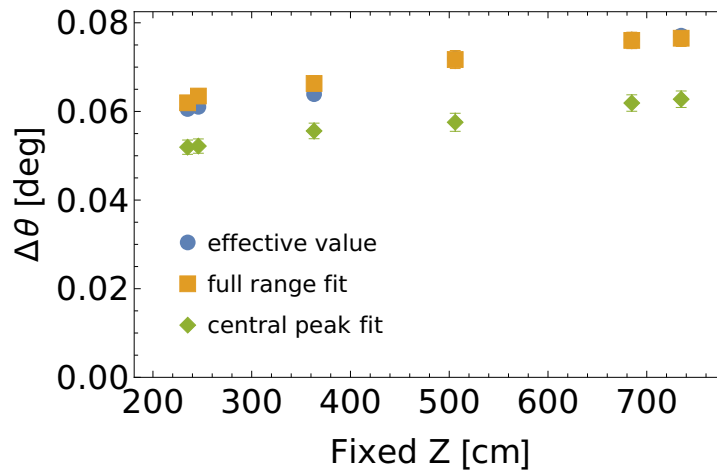


Figure 5: Dependence of the  $\Delta\theta$  resolution on fixed  $z$  in the TSCS for the different stages of the fitting procedure.



the initial, full-range fit. The bottom row of green points are the widths from the fit to the narrow central peak and the middle row of blue points is the combined, effective resolutions. In each case there is a steady increase in the width through the drift chambers, FTOF, and ECAL. The resolutions for the FTOF and ECAL plateau close to the value of DC R3. The ordering of the points at each value of  $z$  are what was expected. The full-range fit (yellow points) has the largest width, the narrow-range fit (green points) is lowest, and the effective width determination (blue points) which is a combination of the first two fits is in between those extremes.

## 6 Results

We now present a representative sample of the results from our study of the reconstruction resolution. The full set is in the appendix. In the first set of plots, Figs 6 - 8 we show the change of the resolution between *gemc* version 4.4.0 (yellow points) and 4.3.2 (blue points). In upgrading *gemc* considerable effort was made to make the generation of the subsystem signals more realistic. The result shown in Fig. 6 for the  $\Delta x$  and  $\Delta y$  distributions is about a 50% increase in the widths of the distributions at the largest fixed  $z$  in the more recent version of *gemc*. This is a significant effect. These changes to the simulation make *gemc* more realistic and is part of a wide effort to bring the simulation closer to the data. We also observe the effect increases with increasing fixed  $z$ . Resolution results for  $\Delta z$  and the impact parameter  $b = \sqrt{\Delta x^2 + \Delta y^2}$  are shown

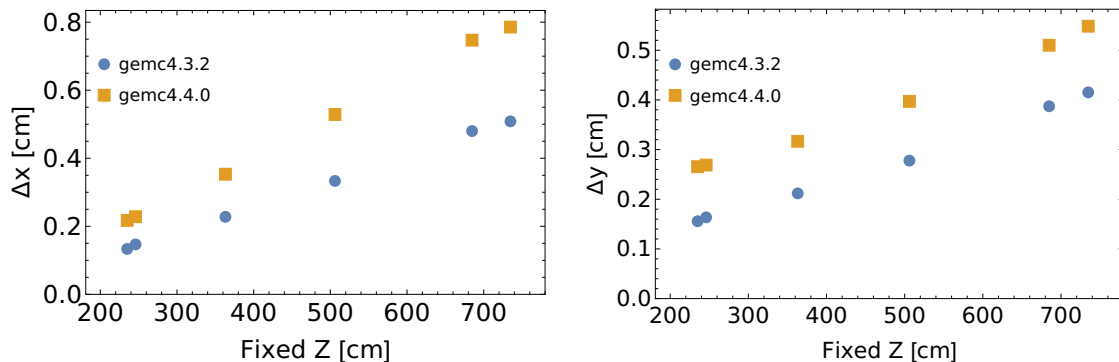


Figure 6: Fit results for the widths of the  $\Delta x$  (left) and  $\Delta y$  (right) distributions for *gemc* version 4.4.0 (yellow points) and 4.3.2 (blue points).

in Fig. 7 and show a similar effect. We see a large increase in the widths of the distributions in updating *gemc* at the same value of fixed  $z$ . The resolution here also increases as the track moves through CLAS12. The final plots in this series are shown in Fig. 8 for  $\Delta\phi$  and  $\Delta\theta$ . Here the widths of the distributions are less sensitive to fixed  $z$  than in Figs. 6 - 7. For  $\Delta\theta$  (rhs of Fig. 8), the increase in the width from *gemc* 4.3.2 to *gemc* 4.4.0 is in the same range at  $\approx 40 - 50\%$ . The results for  $\Delta\phi$  (lhs of Fig. 8) are surprising. The resolution in Region 1 of the DCs (fixed  $z \approx 240$  cm) is worse (larger) than in the other CLAS12 subsystems at larger fixed  $z$  even though the particles have traversed more material. We carefully validated our codes including the algorithms that perform the rotations required for this analysis [9]. This was a period of rapid development of the *gemc* simulation and we suspect there may have been inconsistencies between sub-components of the code as that work progressed.

We expect that multiple scattering will decrease as the energy of the electrons increases [10]. This is seen in Fig 9 which shows the resolution for  $\Delta x$  (left panel) and  $\Delta\theta$  (right panel) for different energies as a function of fixed  $z$ . The widths get smaller as the energy increases from top to bottom at each value of fixed  $z$ . To show the energy dependence more clearly, in Fig. 10 we plot  $\Delta z$  for the drift chamber superlayer 1 (SL1) and the ECAL inner detector layer 4 as functions of the electron energy from 3 GeV to 9 GeV. The widths for these two detectors cover different ranges -  $\Delta x \approx 0.05 - 0.21$  cm for the DC and  $\Delta z \approx 0.26 - 0.81$  cm for the ECAL, but their shapes are similar. Each drops by more than a factor of three in the electron range sampled here as in Fig. 9.

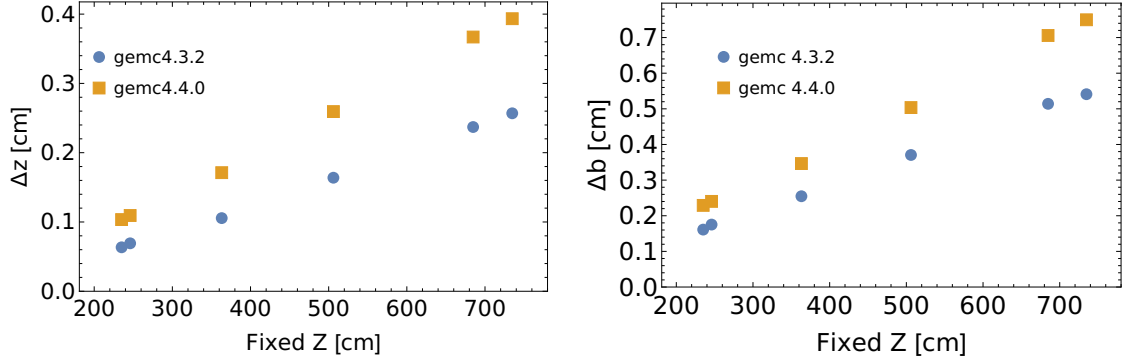


Figure 7: Fits results for the widths of the  $\Delta z$  (left) and the impact parameter  $b$  (right) extracted as  $b = \sqrt{\Delta x^2 + \Delta y^2}$  distributions for *gemc* version 4.4.0 (yellow points) and 4.3.2 (blue points).

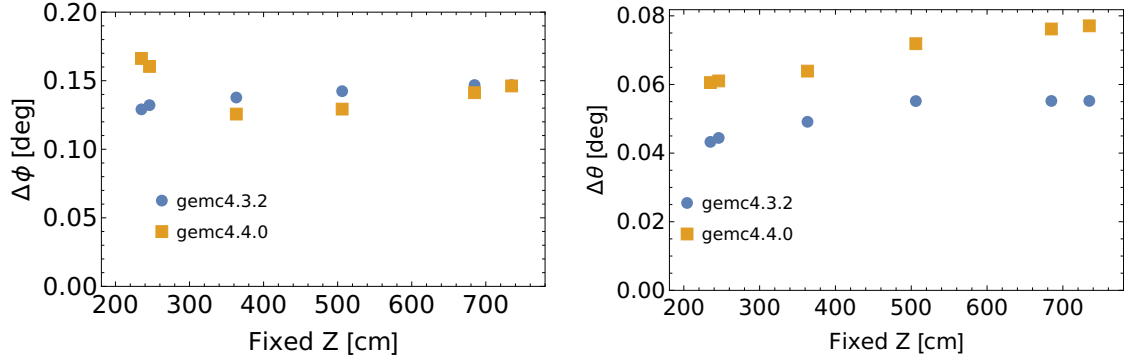


Figure 8: Fits results for the widths of the  $\Delta\phi$  (left) and  $\Delta\theta$  (right) distributions for *gemc* version 4.4.0 (yellow points) and 4.3.2 (blue points).

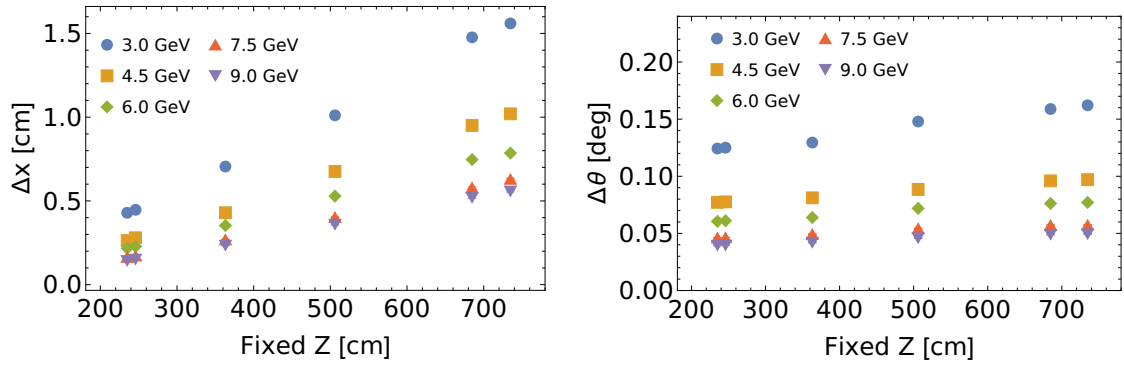


Figure 9: Fits results for the widths of the  $\Delta x$  (left) and  $\Delta\theta$  (right) distributions as a function of fixed  $z$ . The different points at each value of fixed  $z$  represent different electron energies. The energy increases from the top point at each value of fixed  $z$  downward at energies 9.0 GeV (blue), 7.5 GeV (yellow), 6.0 GeV (green), 4.5 GeV (red), and 3.0 GeV (gray).

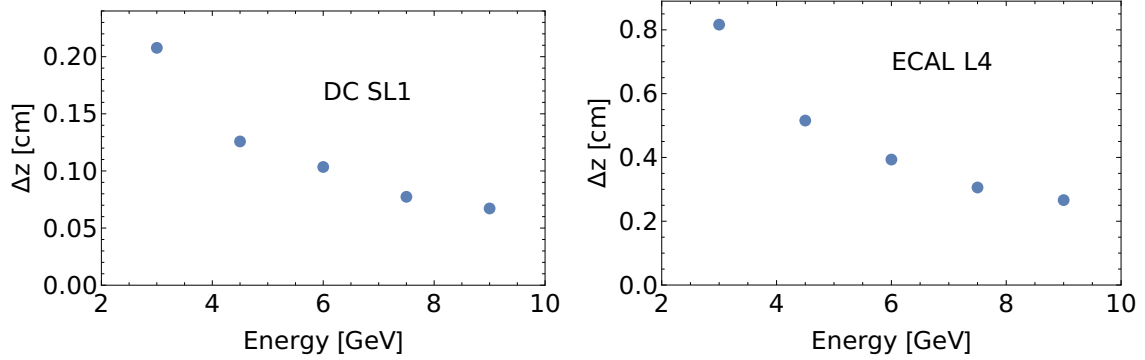


Figure 10: Electron energy dependence of the  $z$  resolution for the DC SL 1 (left panel) and the ECAL inner detector layer 4 (right panel).

We also studied the resolution of the observables for different particle species in *gemc*. In addition to the electron results discussed up to this point, we also ran simulations with negative pions and muons. The results are shown in Fig 11 for  $\Delta z$  and  $\Delta\theta$ . Energy loss by electrons is dominated by bremsstrahlung while

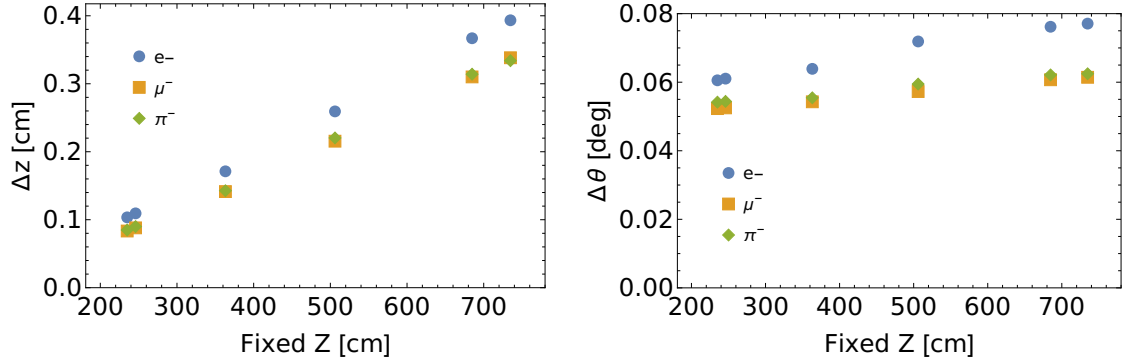


Figure 11: Dependence of the reconstruction resolution on particle type: negative electron (blue), muon (yellow), and pion (green). Particle energy in each case is 6 GeV.

ionization is the main contributor for muons and pions at these energies [10]. Electrons are lighter and radiative corrections have a larger impact and we observed larger tails in the electron distributions. As the particles travel through CLAS12 (and pass through more material) the muon and pion resolutions increase, but remain close to one another. Meanwhile the electron resolution increases more rapidly. For all particle types, there is a significant increase in the width as the particles move through CLAS12.

In Fig. 12 we show the effect of reversing the torus magnetic field polarity and flipping the electron trajectories from inbending to outbending. From small fixed  $z$  (passage through small amounts of material) to large values of fixed  $z$  (passage through large amount of material) the widths of the  $\Delta x$  and impact parameter  $b$  distributions increase modestly.

Table 4 shows the HTCC results. The HTCC resolutions are not included in the plots of the other subsystem results because a different swimmer method was used that uses the lab coordinates.

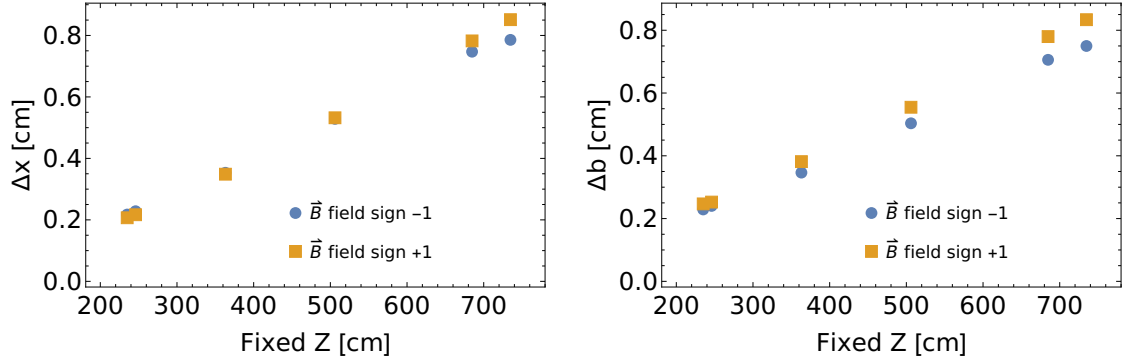


Figure 12: Effect of reversing the torus field current on electrons at 6 GeV for  $\Delta x$  and impact parameter  $\Delta b$  resolutions.

Event File	$\Delta x$	$\Delta y$	$\Delta z$	$\Delta\phi$	$\Delta\theta$	$\Delta b$
6 GeV $e^-$	0.14224	0.26871	0.07216	0.22496	0.05920	0.15909
6 GeV $\mu^-$	0.12067	0.21764	0.06148	0.16634	0.05163	0.13992
6 GeV $\pi^-$	0.12526	0.21754	0.06331	0.16682	0.05357	0.14468
3 GeV $e^-$	0.28961	0.33924	0.14639	0.26645	0.12423	0.32176
4.5 GeV $e^-$	0.18046	0.28126	0.08919	0.22661	0.07654	0.20067
7.5 GeV $e^-$	0.11233	0.23361	0.05276	0.20878	0.04620	0.12354
9 GeV $e^-$	0.09898	0.23964	0.04590	0.20245	0.03956	0.10431
6 GeV $e^-$ , RGA	0.12321	0.22838	0.06196	0.21298	0.04767	0.14088
6 GeV $e^-$ , RGB	0.12073	0.22626	0.05995	0.21518	0.04702	0.13936
6 GeV $e^-$ , $t = +1$	0.13673	0.28365	0.06753	0.25740	0.05934	0.16224

Table 4: HTCC results. In the first column  $t$  refers to the torus polarity and RGA and RGB refer to different CLAS12 run periods with different reconstruction parameters.

## 7 Conclusion

We have measured the CLAS12 reconstruction resolution in simulation for a variety of particle species, energies, kinematics, torus polarities, geometries, and software versions. The results can be used as benchmarks for the performance of the software and hardware elements of the CLAS12 subsystems. They can also be used to improve the accuracy of the calculation of the covariance matrix in the CLAS12 reconstruction code. By and large the results followed the expectations for the qualitative behavior of the resolution and provided a more quantitative grounding. We did see a large ( $\approx 40 - 50\%$ ) increase (worsening) in the resolution in a more recent version of the CLAS12 Monte-Carlo simulation code *gemc* which reflects a wide effort to make the simulation of the subsystem signals more realistic.

## References

- [1] V. D. Burkert et al. The CLAS12 Spectrometer at Jefferson Laboratory. *Nucl. Instrum. Meth.*, A959:163419, 2020.
- [2] V. Gyurjyan, D. Abbott, G.P. Gilfoyle, J. Carbonneau, G. Heyes, S. Paul, C. Timmer, D. Weygand, and E. Wolin. CLARA: A Contemporary Approach to Physics Data Processing. *J.Phys.Conf.Ser.*, 331, 2011.
- [3] V. Gyurjyan, S. Mancilla, and R. Oyarzún. CLARA: CLAS12 Reconstruction and Analysis Framework. *J. Phys. Conf. Ser.*, 762(1):012009, 2016.
- [4] V. Ziegler et al. The CLAS12 software framework and event reconstruction. *Nucl. Instrum. Meth.*, A959:163472, 2020.
- [5] M. Ungaro et al. The CLAS12 Geant4 simulation. *Nucl. Instrum. Meth. A*, 959:163422, 2020.
- [6] S. Agostinelli et al. GEANT4—a simulation toolkit. *Nucl. Instrum. Meth. A*, 506:250–303, 2003.
- [7] CLAS12 Javadocs. <https://clasweb.jlab.org/clas12offline/docs/javadoc/>.
- [8] L. Trailovic and L.Y. Pao. Variance Estimation and Ranking of Gaussian Mixture Distributions in Target Tracking Applications. page 2195, 2002.
- [9] R. Sanford, A. Saina, V. Ziegler, and G.P. Gilfoyle. Analysis and Validation of Reconstruction Resolution for CLAS12. In *Bull. Am. Phys. Soc., Fall DNP Meeting*, 2021. GA.00012.
- [10] N. Tanabashi et al. Review of particle physics. *Phys. Rev. D*, 98:030001, 2018.

## APPENDIX

The default configuration of the simulations is electrons at 6 GeV, gemc 4.4.0, default/ideal geometry, sector 1, and function of fixed  $z$  in the Tilted Sector Coordinate System (TSCS). The labels on each plot will identify the parameter values associated with each data set.

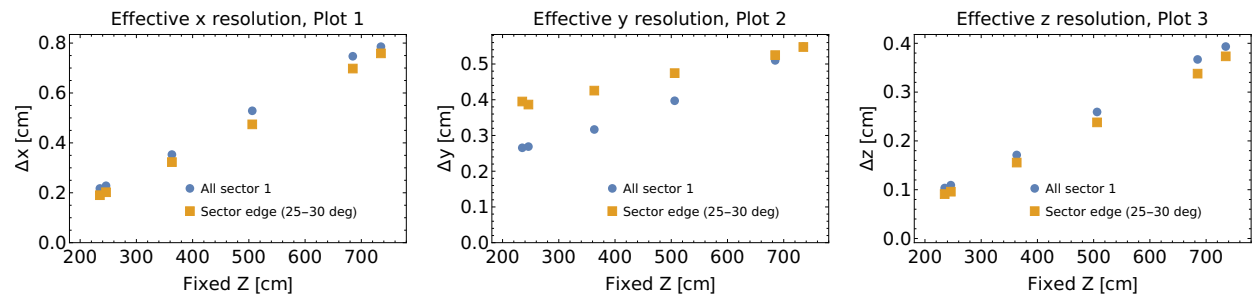


Figure A.1

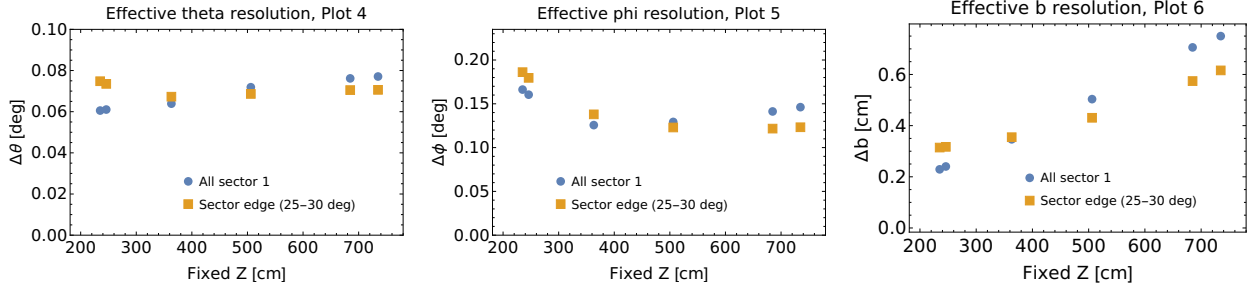


Figure A.2

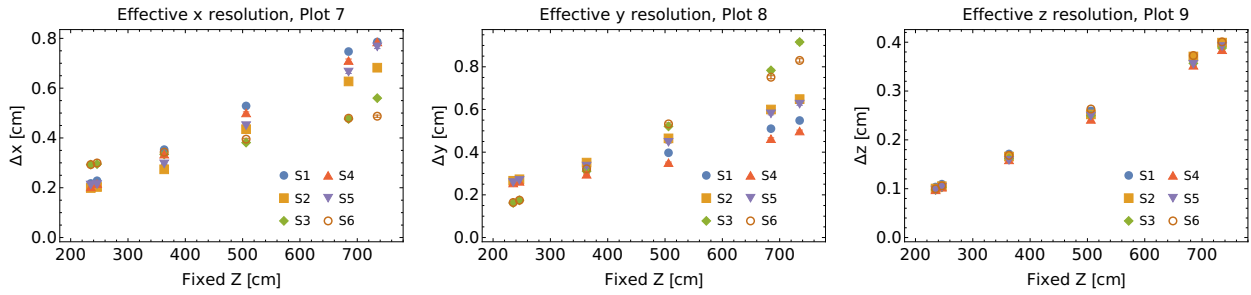


Figure A.3

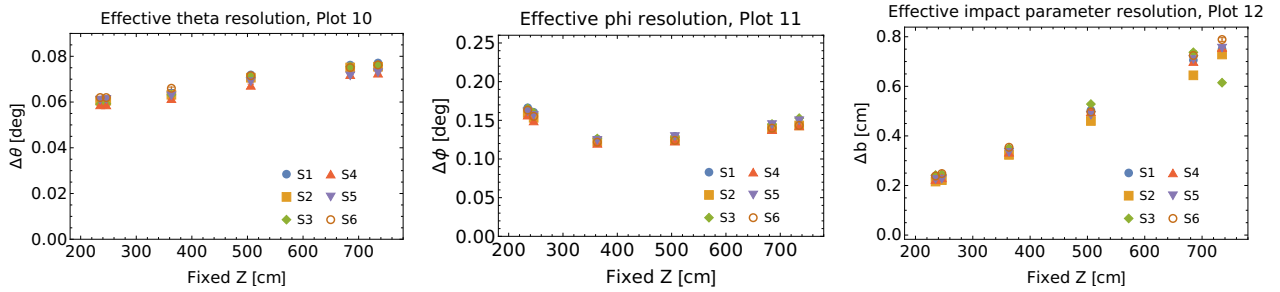


Figure A.4

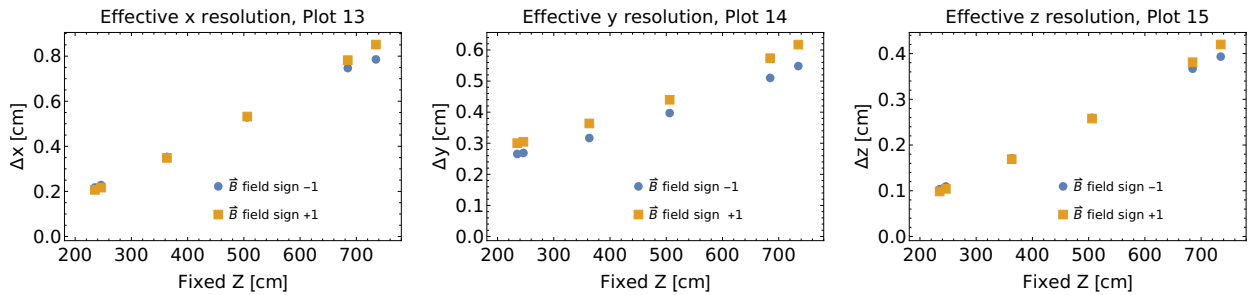


Figure A.5

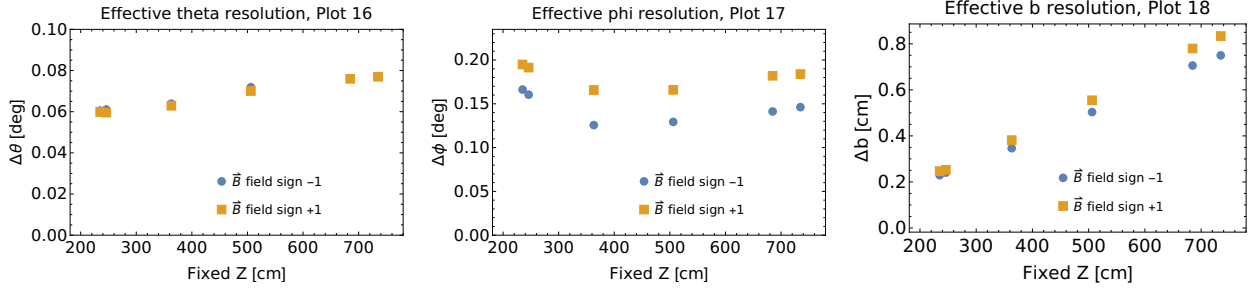


Figure A.6

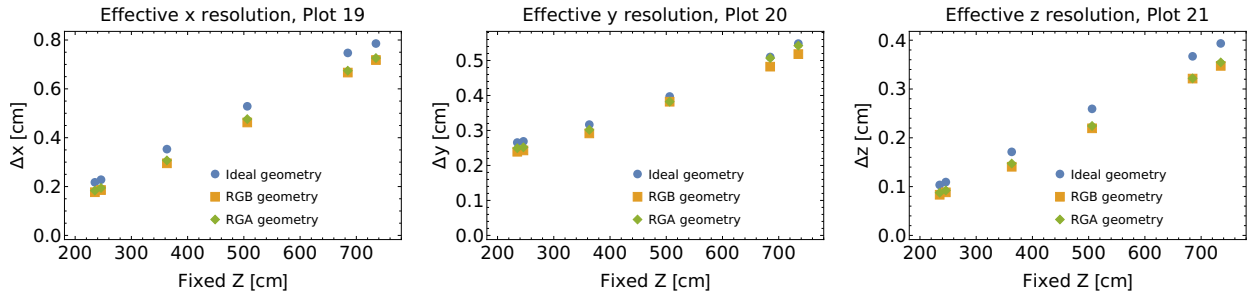


Figure A.7

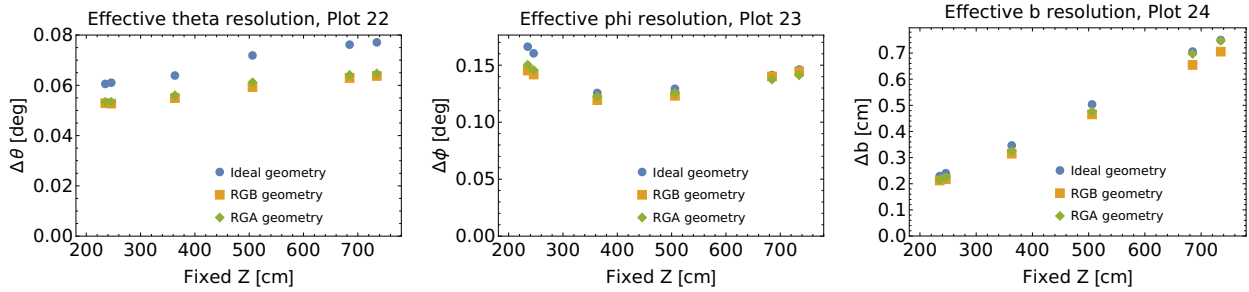


Figure A.8

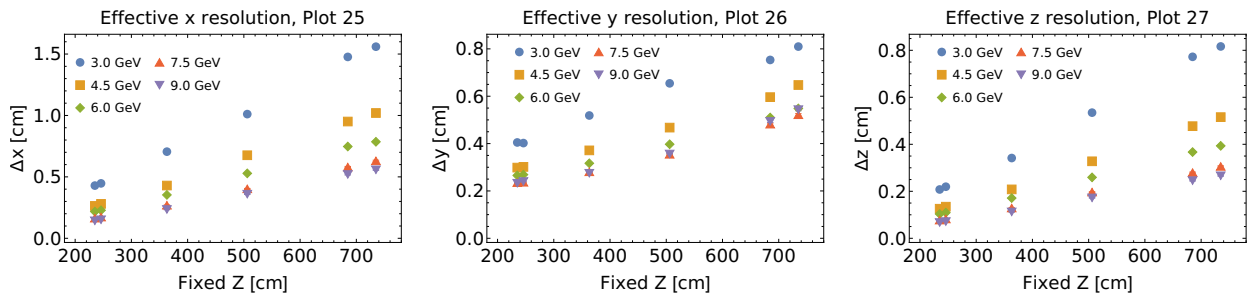


Figure A.9

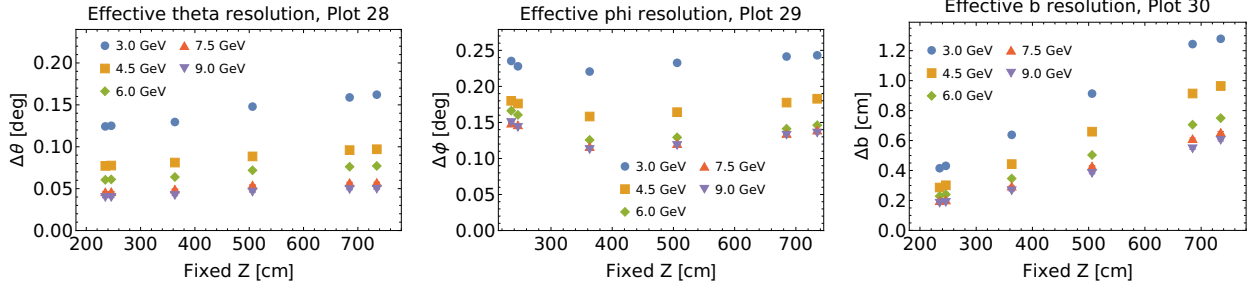


Figure A.10

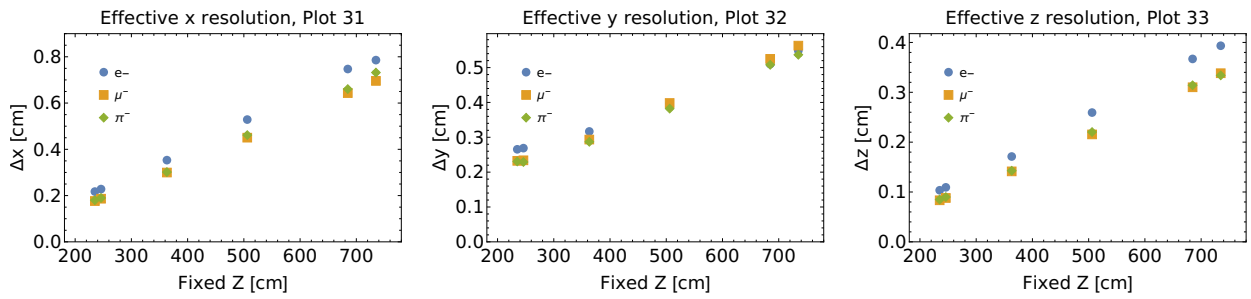


Figure A.11

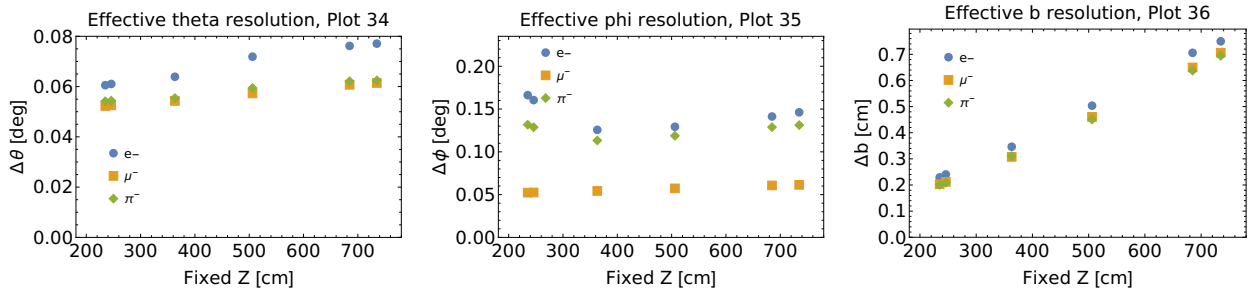


Figure A.12

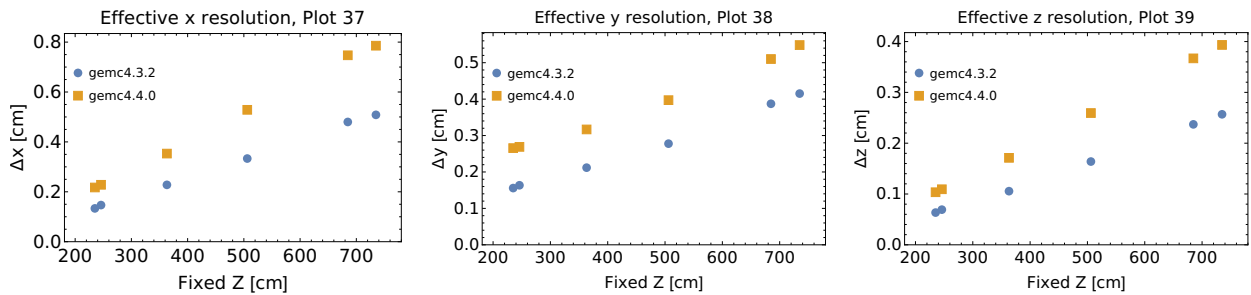


Figure A.13



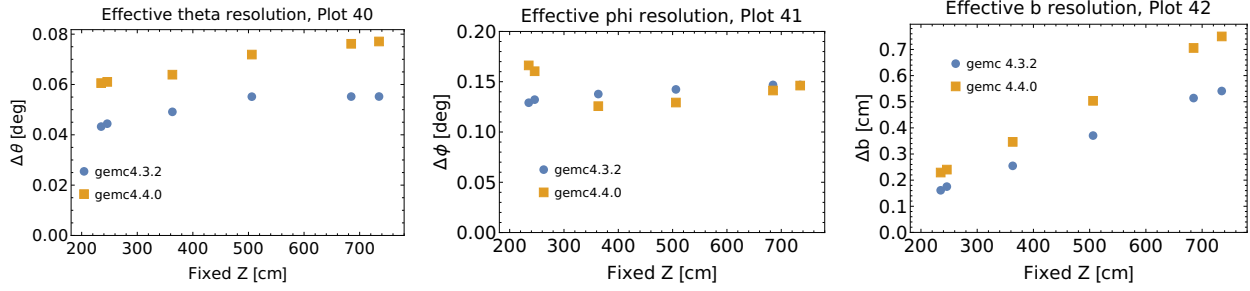


Figure A.14

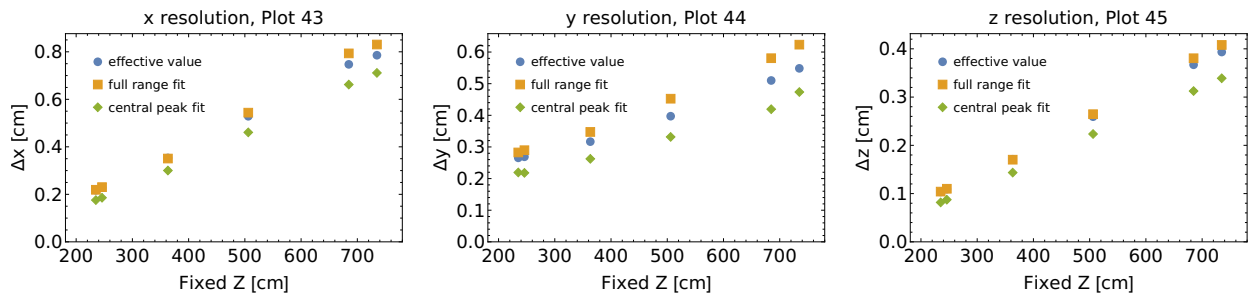


Figure A.15

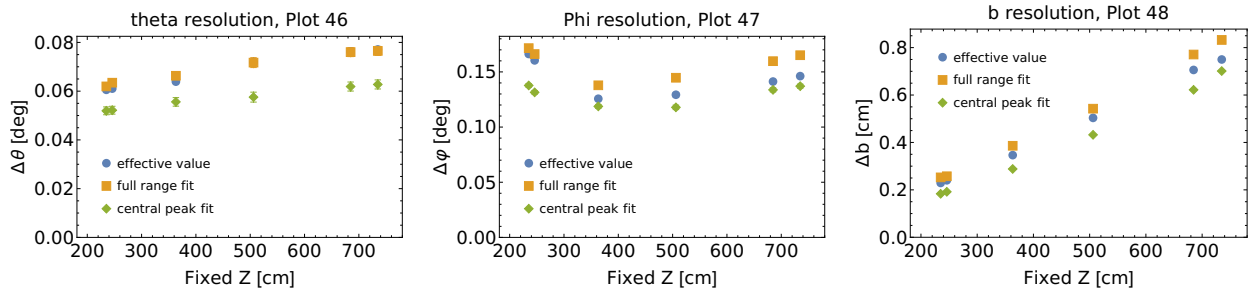


Figure A.16

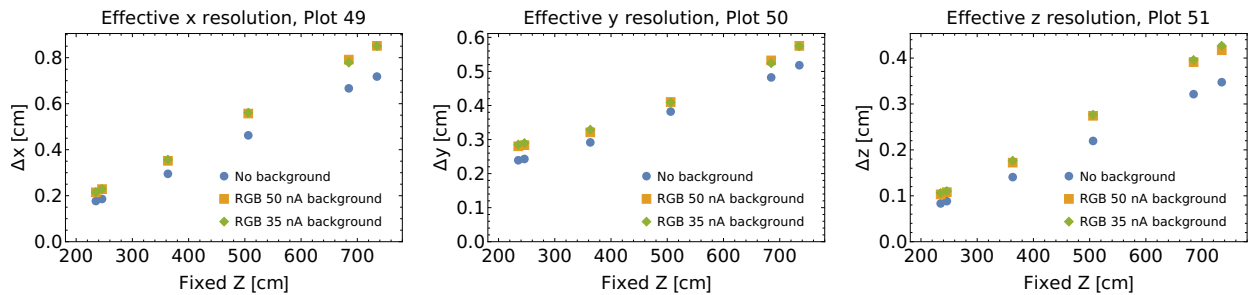


Figure A.17

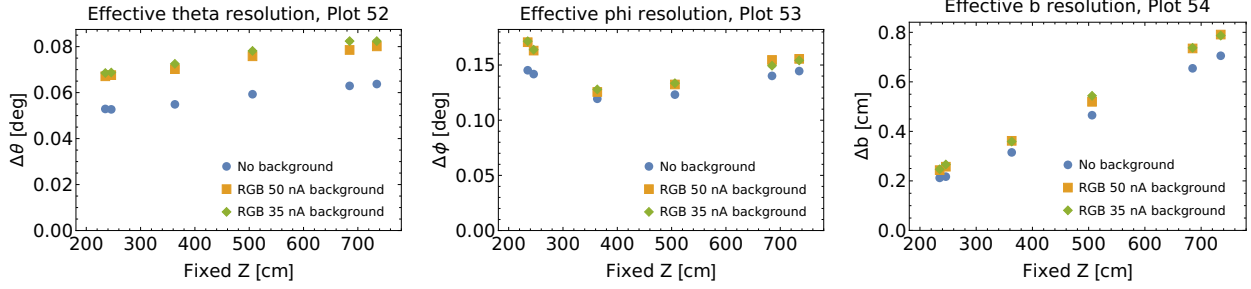


Figure A.18

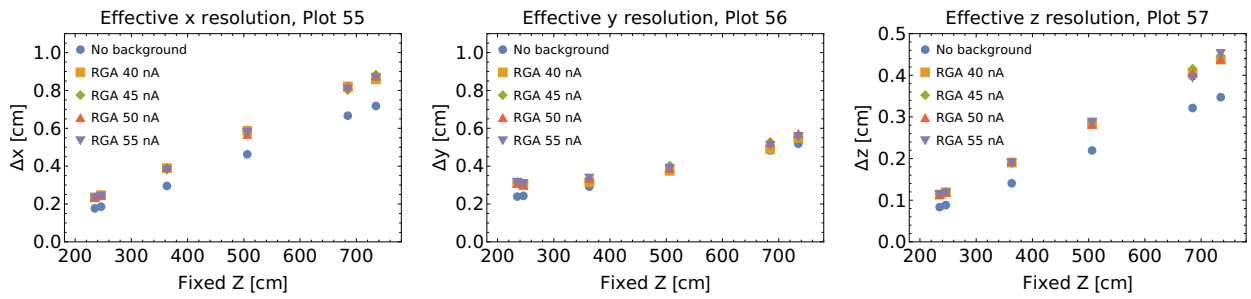


Figure A.19

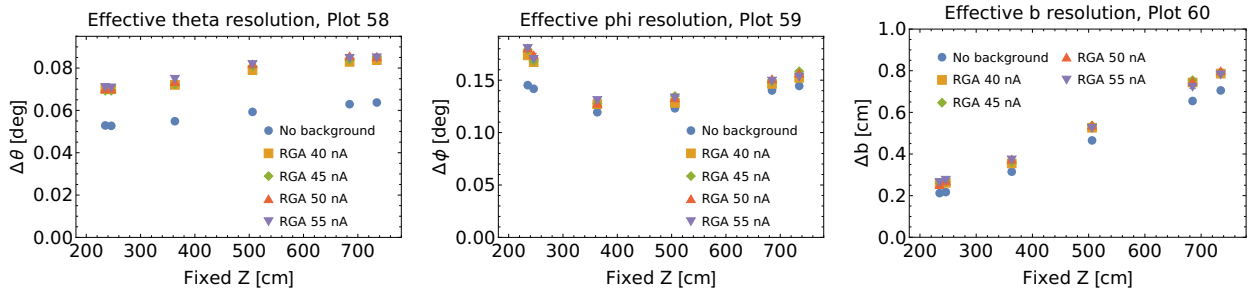


Figure A.20

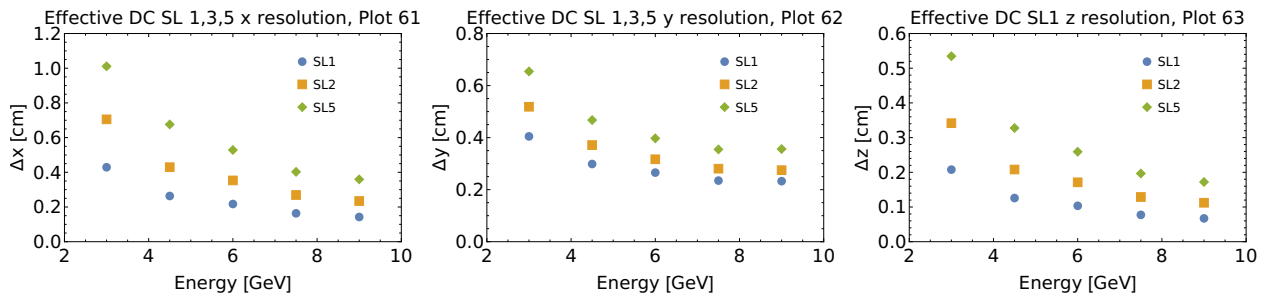


Figure A.21

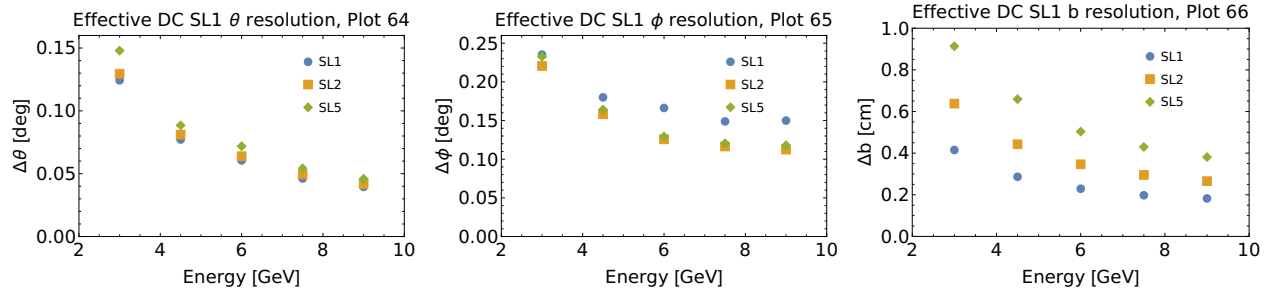


Figure A.22